Supporting Information

Photoelectrochemical water splitting by triazine based covalent organic framework

Anirban Pradhan,*,[†] Matthew A. Addicoat,[¶]

[††] *Department of Chemistry, Birla Institute of Technology (BIT) – Mesra, Ranchi, Jharkhand, 835215, India.*
[¶]*School of Science and Technology, Nottingham Trent University, Clifton Lane, Nottingham, NG11 8NS, UK.*

Experimental section:

Materials:

All reagents were supplied from best available commercial sources and were used without further purification. 1,3,5-tris (4-formylbiphenyl) benzene (TFBB), 2, 4, 6-Tris(4-aminophenyl)-1, 3, 5-triazine (TAT) and 2, 4, 6-Tris(4-aminophenyl)-benzene (TAB) were synthesized by previously reported procedure. Pd charcoal (Pd/C), Tetrakis (triphenylphosphine) palladium (0) was received from sigma Aldrich. 4-fromyl phenyl boronic acid, *n*-butanol (*n*-BuOH), *o*-dichlorobenzene (*o*-DCB) *etc*. were purchased from Spectrochem, India. Other solvents, acid, bases were supplied from the local commercial source.

Methods:

Synthesis of 1,3,5-tri(4-formylbiphenyl)benzene (TFBB) and 2,4,6-tris(4-aminophenyl)-1,3,5-triazine (TAT) compound was followed previously reported procedure.[1]

Synthesis of TFBB-TAT and TFBB-TAB COF:

A mixture of o-Dichlorobenzene (*o*-DCB) & *n*-butanol (1:1, 3ml) was purged in a schlenk tube (6 inch × 22 mm) with a mixture of TFBB (0.3 mmol, 185.6 mg) & TAT (0.3mmol, 106.2 mg) for TFBB-TAT COF and TFBB (0.3 mmol, 185.6 mg) & TAB (0.3mmol, 105.4 mg) for TFBB-TAB COF. 0.2 ml (6M) acetic-acid catalyst was added to the mixture and sonicated for 1h. Then the tube was degassed via freeze-pump-thaw cycles for three times and flame sealed under vacuum. The tube was then heated statically at 120 °C for 3 days. The yellow precipitate was collected via centrifugation, washed several times with dimethylacetamide (DMAC), tetrahydrofuran (THF) and dry acetone to remove the trapped guest molecules. The powder was collected and dried at 120 °C under vacuum overnight to form TFBB-TAT and TFBB-TAB COF in an isolated yield of 90% and 95% respectively.

Instrumentations:

Powder X-ray Diffraction (PXRD): Powder X-Ray diffraction patterns of the powder samples were obtained with a Bruker AXSD-8 Advanced SWAX diffractometer using Cu-Kα (0.15406 nm) radiation. The powder samples were put on a silica holder and placed on the sample holder. The experimental data was collected from 2θ value of 2° to 40° with a scan rate of 3 sec/step.

Transmission Electron Microscopy (TEM): High resolution TEM (HR-TEM) images were taken on a UHR-FEG-TEM, JEOL, JEM 2100 F model using 200 kV electron source. The

samples were first dispersed in isopropanol and then drop casted on a carbon-coated copper grid and the grid was dried in vacuum.

Scanning Electron Microscopy (SEM): Scanning electron microscopic analysis was performed with a JEOL JEM 6700F field-emission scanning electron microscope (FESEM).

Fourier Transmittance Infrared spectroscopy (FT-IR): FT-IR spectra of the synthesized samples were recorded using a Nicolet MAGNA-FT-IR 750 Spectrometer Series II.

Surface area analysis (BET): N_2 adsorption/desorption isotherms of the sample was recorded using an AutosorbiQ instrument (ASiQin version 5.0) at 77 K. The sample was first degassed at 120 $^\circ$C for overnight and set for measurement. Pore size distribution (PSD) was calculated by using NLDFT considering the carbon/slit-cylindrical pore model.

^{1}H and ^{13}C NMR:

Solid State Cross Polarisation ^{13}C Magic Angle Spinning (ssCP-MAS) NMR: Solid state ^{13}C CP-MAS NMR spectrum of TFBB-TAT and TFBB-TAB COF were recorded in a 500 MHz BrukerAvance III spectrometer at a MAS frequency of 10 kHz.

X-ray photoelectron spectroscopy (XPS): The samples were first dispersed in isopropanol and sonicated for 1hr. The dispersed sample was then dropcasted on a cleaned glass surface and the solvent was removed by vacuum. A thin film was formed on the glass surface.

Photoelectroectrochemical measurement:

All the electrochemical measurements were executed with a standard three electrode setup using a CHI 660D potentiostat. The three electrode setup consists of an active material containing bare or PEDOT : PSS modified ITO substrate as working electrode along with saturated calmel electrode (SCE) and Pt wire as reference and counter electrode respectively. The working electrode was fabricated by depositing COF slurry on the bare or modified ITO substrate. The COF slurry was prepared by dispersing COF powder in ethanol by sonication followed by addition of 10 wt% Nafion as binder. Subsequently, the COF slurry was coated on the bare or modified ITO substrate by drop casting. Prior to the working electrode fabrication the ITO surface was modified with PEDOT : PSS layer using spin coating. The PEDOT : PSS layer coated ITO substrate was dried in a vacuum oven at 80 ºC for 2h. All electrochemical studies were carried out in 0.5 M Na_2SO_4 aqueous solution. The photoelectrochemical measurements were carried out under simulated solar light irradiation emitted from a 300 W Xenon arc lamp equipped with a 420 nm cutoff filter. The linear sweep voltammograms (LSV) were recorded at 10 mV/s scan rate within a potential window of 0.2

to -0.8 V vs SCE. The transient photocurrent response was measured at -0.5 V in the same electrochemical setup. The electrochemical impedance of the designed photocathodes was measured in a frequency range of 1 Hz to 10 kHz with a sinusoidial perturbation signal of 5 mV. Photoelectrochemical water to hydrogen production was carried out by chronoamperometry.

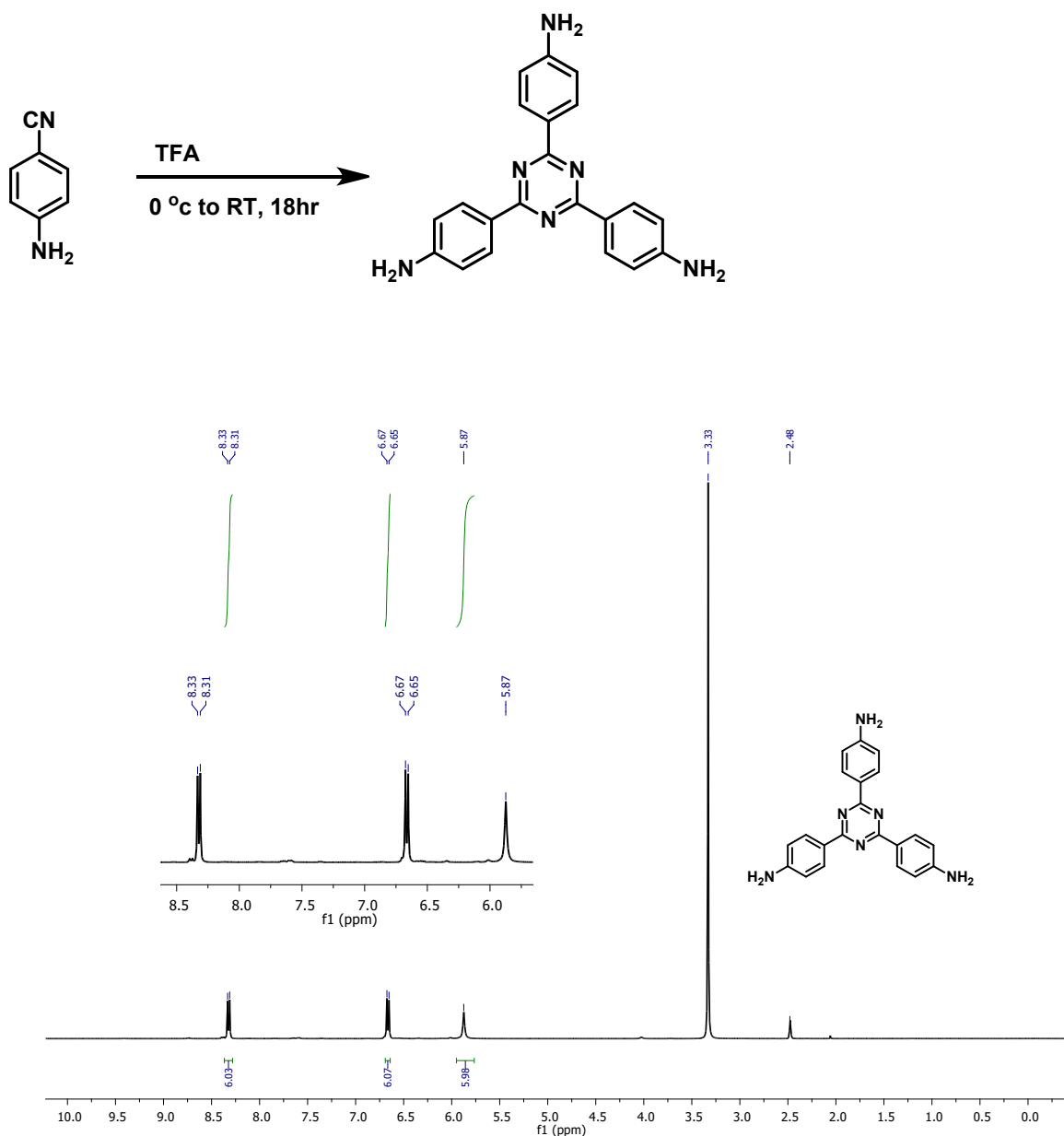***Synthesis of 2, 4, 6-tris (4-aminophenyl)-1, 3, 5-triazine (TAT)***

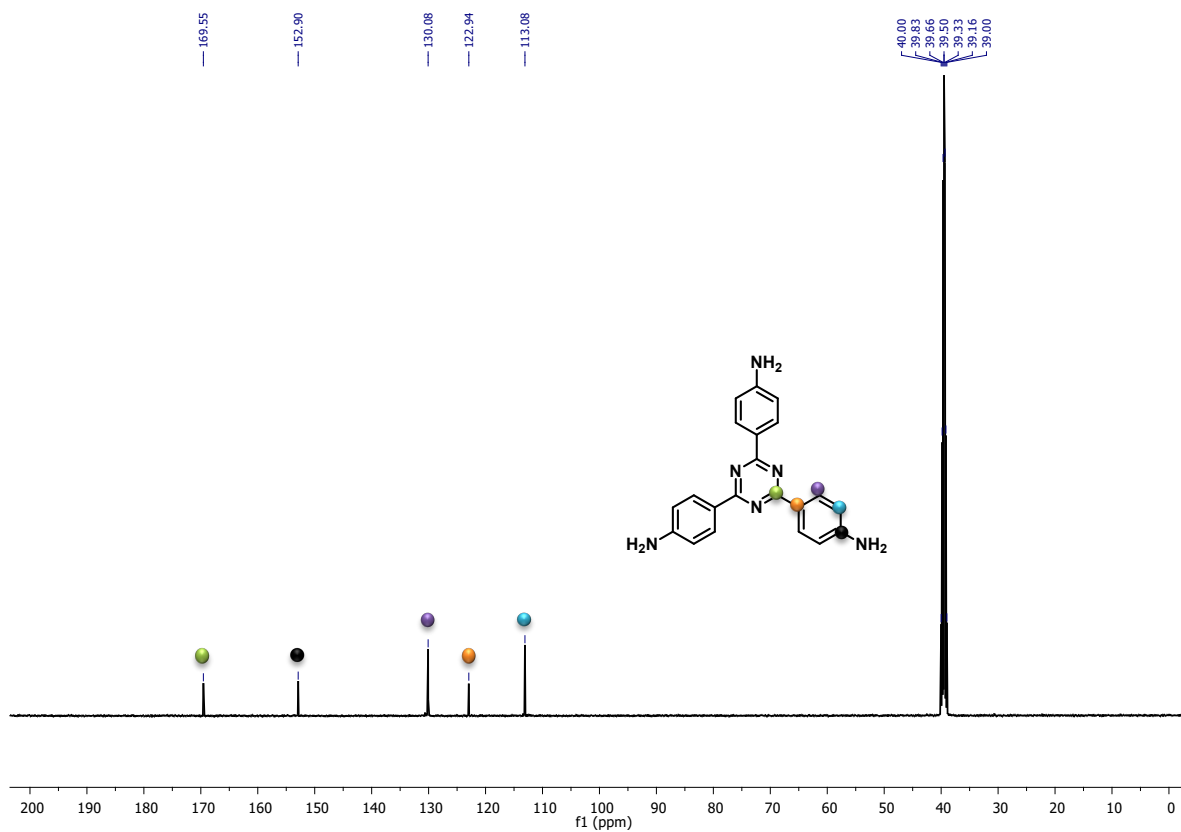**Figure S1.** ^{1}H NMR of 2, 4, 6-tris (4-aminophenyl)-1, 3, 5-triazine (TAT).

Figure S2. ^{13}C NMR of 2, 4, 6-tris (4-aminophenyl)-1, 3, 5-triazine (TAT).
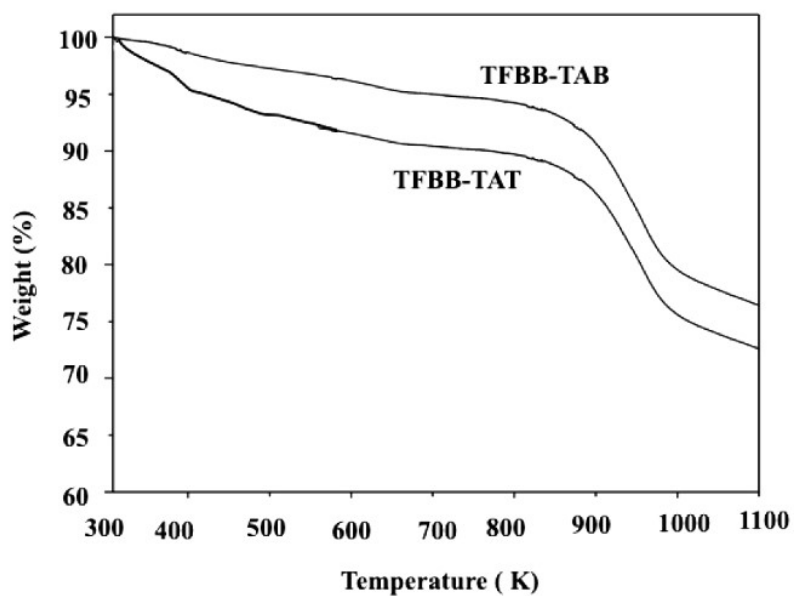

Figure S3. Thermogravimetric analysis (TGA) of TFBB-TAB and TFBB-TAT COF.
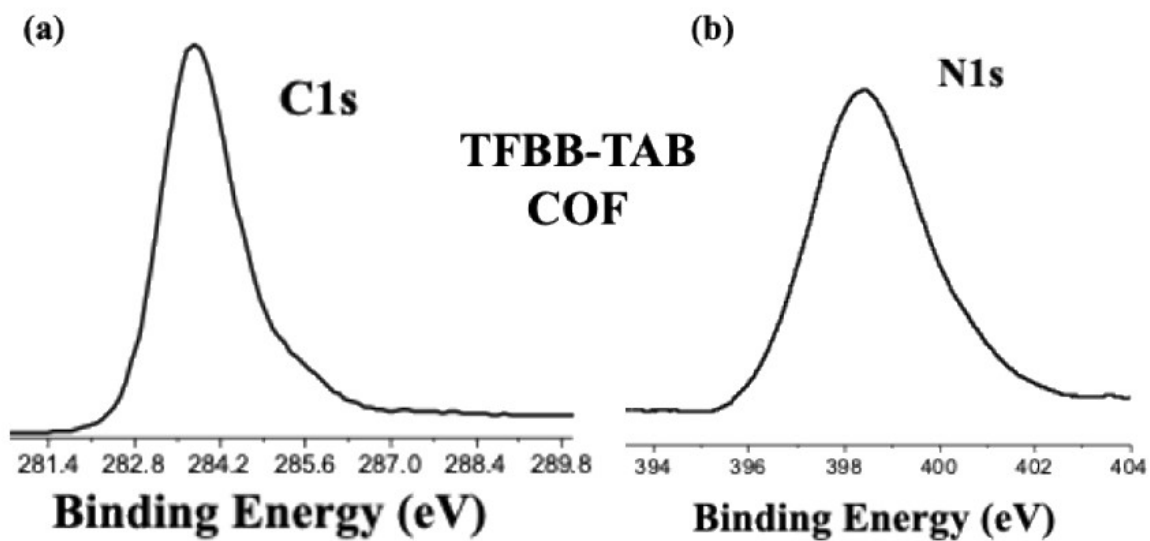
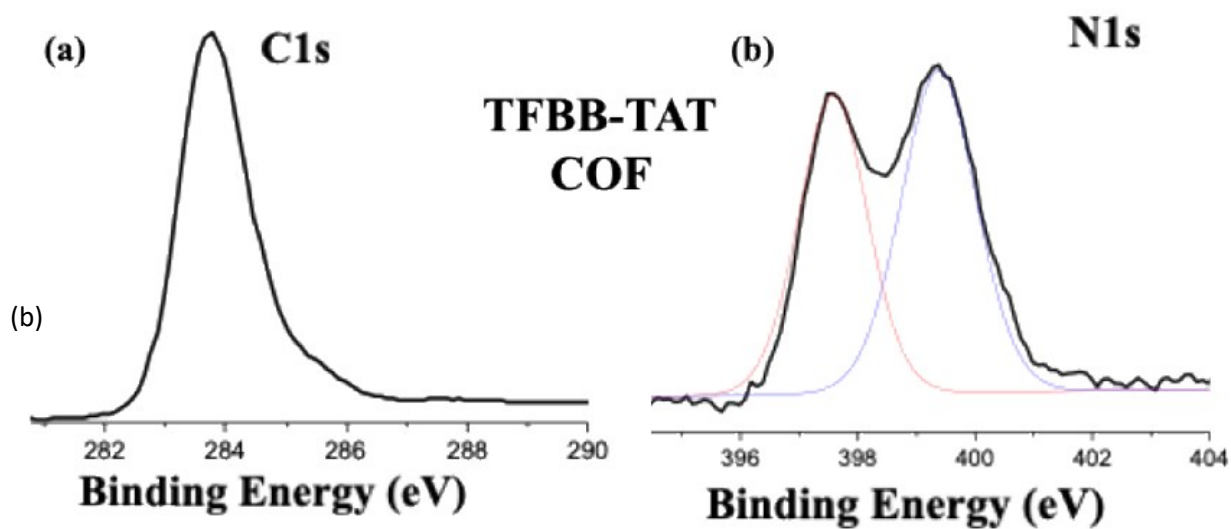**Figure S4**: (a) C 1s region XPS spectrum, (b) N 1s region XPS spectrum of TFBB-TAB.

Figure S5: (a) C 1s region XPS spectrum, (b) N 1s region XPS spectrum of TFBB-TAT.
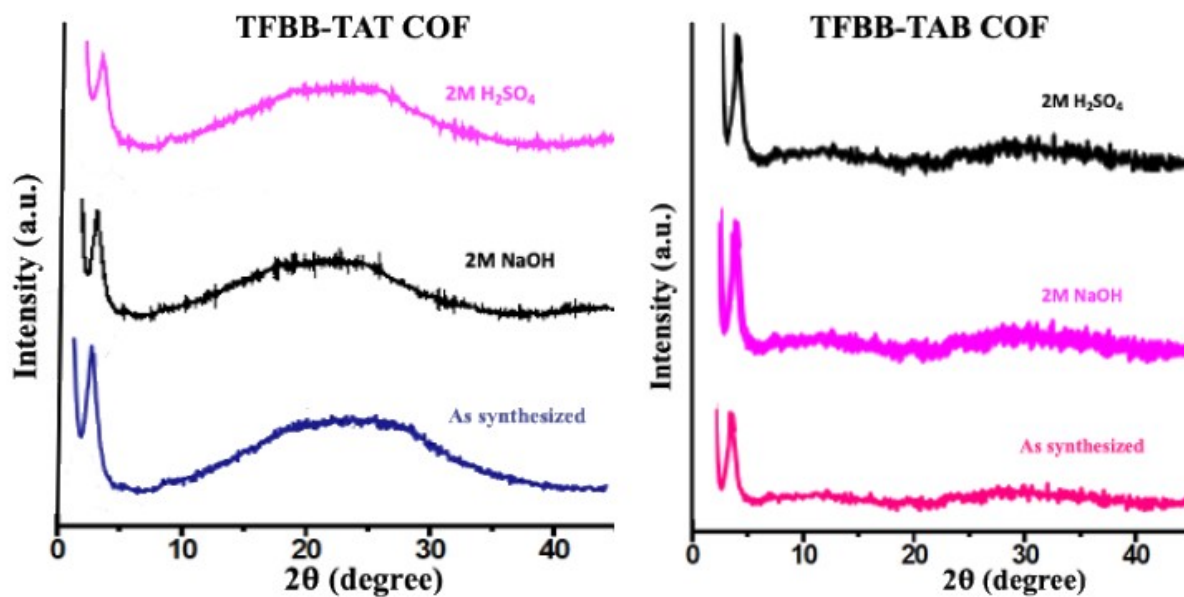
Figure S6. XRD patterns of (a) TFBB-TAT and (b) TFBB-TAB COF after treatment in different conditions. NaOH (2M) and H2SO4 (2M)

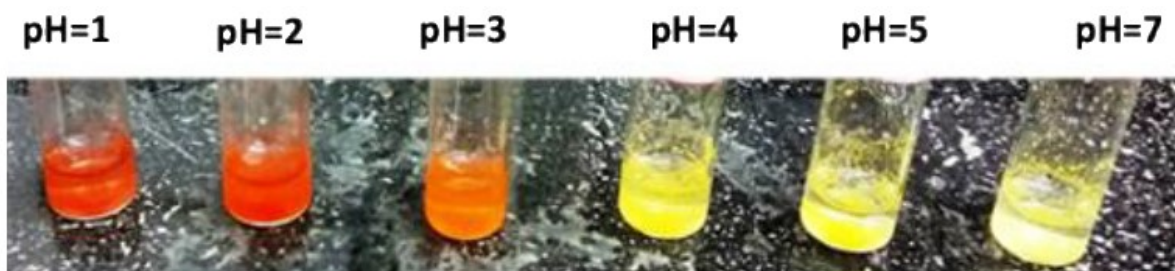**Acid Responsive Covalent Organic Frameworks:**

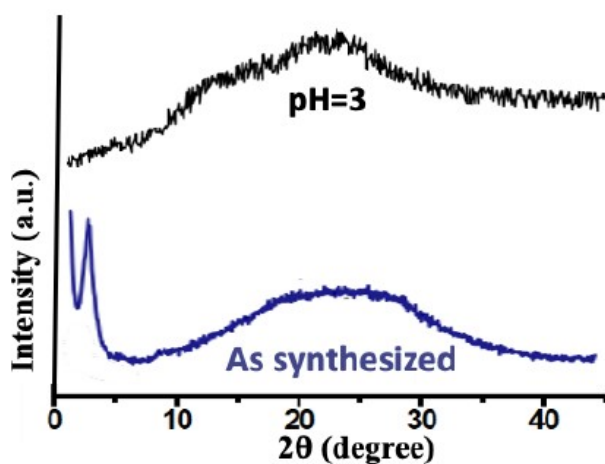**Figure S7**: pH responsive colour change of TFBB-TAT COF material

Figure S8. XRD patterns of (a) TFBB-TAT COF and (b) TFBB-TAB COF at pH 3.

Imine to amine conversation of TFBB-TAT COF: We prepared post synthetic modification of imine to amine of TFBB-TAT COF material following the protocol mentioned in this article (**J. Am. Chem. Soc. 2021, 143, 9, 3430–3438**). We have taken a suspension of TFBB-TAT COF (10.0 mg) in mesitylene (666 μL) and 1,4-dioxane (333 μL), formic acid (97%, 50.0 μL) was added. The suspension was stirred at 120°C for 72 h for the maximum conversion of imine to amine. The precipitate was collected via suction filtration, washed with water, MeOH, DMF, THF, and DCM and dried under high vacuum. Finally, we obtained a yellow solid of imine to amine converted (9.8 gm) TFBB-TAT COF. Fourier transform infrared spectroscopy (FTIR) revealed that after modification, a new vibration band appeared at 3300-3400 cm^{-1} which attributed to a secondary amine (v_{N-H}) stretching mode. The intensity of the imine vibration ($v_{C=N}$) at 1697 cm^{-1} gradually disappeared over prolonged reaction time at 120 °C (**Figure S9**)
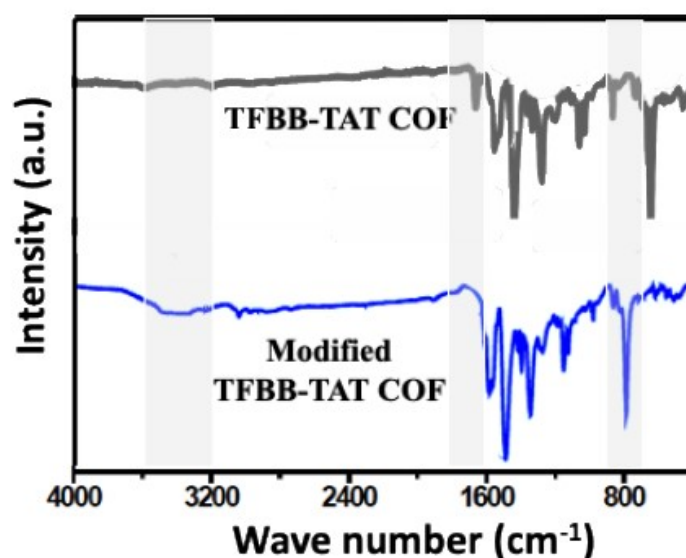

Figure S9. FTIR spectra of TFBB-TAT COF and imine to amine modified TFBB-TAT COF

Electrode Potentials at Different pH:

The applied potential is strongly related to the thermodynamics and kinetics of water photoelectrolysis. The electrode potential of hydrogen evolution reaction and oxygen evolution (HER & OER) through water splitting is dependent on pH in the aqueous solution as expressed by the Nernst equation at 25°C.

$$E(O_2/H_2O)=E°(O_2/H_2O)-(RT/4F)\ln 1/[H^+]^4 = 1.23-0.059pH \text{ [V vs. SHE]}$$

The potential of HER is negatively shifted with a slope of 57 mV per pH unit at 25°C. Thus, the theoretical voltage for water splitting reaction ($\Delta E° = 1.23$ V) is not dependent on pH value.
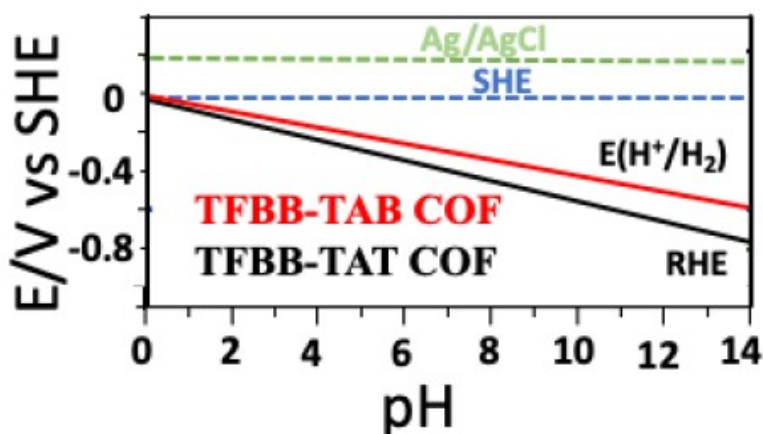

Figure S10: pH dependence of the electrode potentials at 25°C

The following figure emphasize pH dependence of the electrode potentials at 25°C. The potentials of Ag/AgCl reference electrode and SHE are constant, but the potentials of RHE and the potentials for HER of TFBB-TAT and TFBB-TAB COF are linearly increased with the increase of pH value with a slope of 57 mV (ln10 × RT/F) at 25°C.

Photoelectrochemical oxygen evolution reaction:

For the electrocatalytic OER at anode requires overpotentials (η) relative to standard electrode potential $E°(O_2/H_2O) = 1.23$ V vs. RHE. So the overpotential should be higher than 0.2 V at least. OER involves multielectron/proton ($4e^-/4H^+$) transformation ($2H_2O \rightarrow O_2 + 4H^+ + 4e^-$), which needed high activation energy. In the case of PEC reaction for HER at cathode also requires η relative to $E°(H^+/H_2) = 0$ V vs. RHE. The applied electric bias can be reduced In the case of the PEC reaction through the photon energy. We observed oxygen evolution reaction (OER) at photoanode occurs through PEC reaction without applied electric bias (Figure S8).
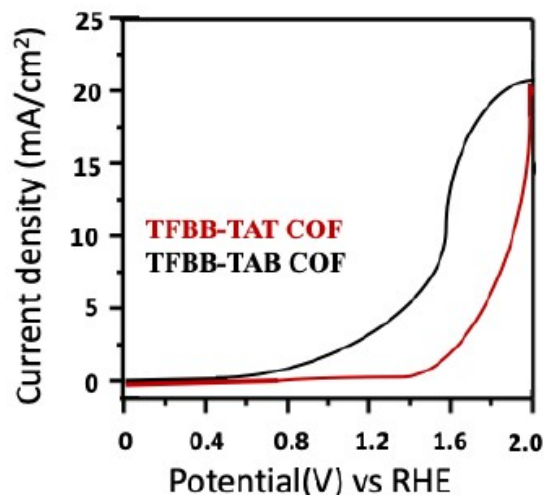
Figure S11: Current-potential curves for photo electrocatalytic water splitting using photoanodes for OER and a cathode for HER at the current density (j) of 2 mA/cm². Under bias free condition.
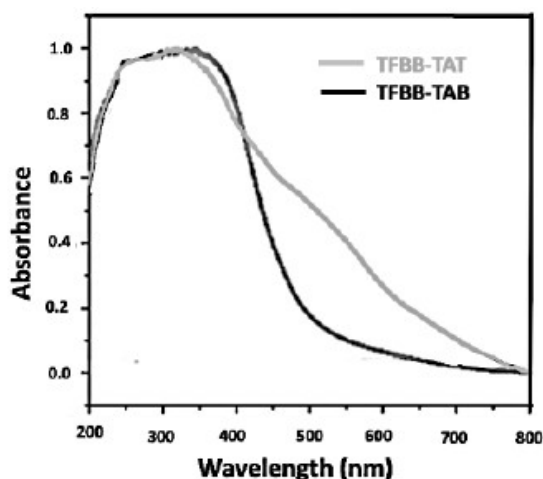

Figure S12: Solid state UV-VIS spectrum of TFBB-TAT and TFBB-TAB COF

The photon energy, hv[eV], can be calculated from light wavelength, λ[nm] by using the following eqation. (A. Fujishima, K. Honda, *Nature* **1972**, *238*, 37-38.)

$$hv \ [eV]=1240 / \lambda \ [nm]$$

The band gap of TFBB-TAT and TFBB-TAB COF has been estimated from the solid state UV-VIS diffuse spectrum (Fig. 5B). This spectrum showed the absorption maxima λ_{max} for TFBB-TAT at ca. 540 nm with calculated band gap of 2.31 eV Which is very close to theoretical band gap (2.38 eV) for slip-AA stacking mode. In the case of TFBB-TAB showed λ_{max} at ca. 430 nm as a result calculated optical band gap of 2.88 eV which is little higher compared to theoretical band gap (2.29 eV) for slip-AA stacking. Visible absorption of

TFBB-TAT and TFBB-TAB COF together with π-conjugation could be helpful in exploring the conducting properties of this COF material.

Theoretical Calculations: Computational details of powder X-ray diffraction for TFBB-TAT and TFBB-TAB COF.

Atomic positions and cell sizes of TFBB-TAT and TFBB-TAB COF layers were optimized using the Self-Consistent-Charge Density-Functional Tight-Binding (SCC-DFTB) method as implemented in DFTB+ version 19.1.[2] All pairwise atomic interactions (C, H, N) were treated using the mio-0-1 parameter set[3] and dispersion was accounted for using UFF dispersion. It is known that the layer stacking is affected by the Coulomb repulsion between the partial atomic charges in adjacent layers.[4] Hence, several slipped AA stacking possibilities were considered for each COF by shifting adjacent layers with respect to each other in different directions (x, xy, y) up to 6Å in addition to eclipsed (AA) and staggered (AB) geometries. Each starting geometry was fully optimized without constraints (P1 space group). The predicted slipped structure has the lowest energy, while maintaining agreement with the experimental PXRD pattern.
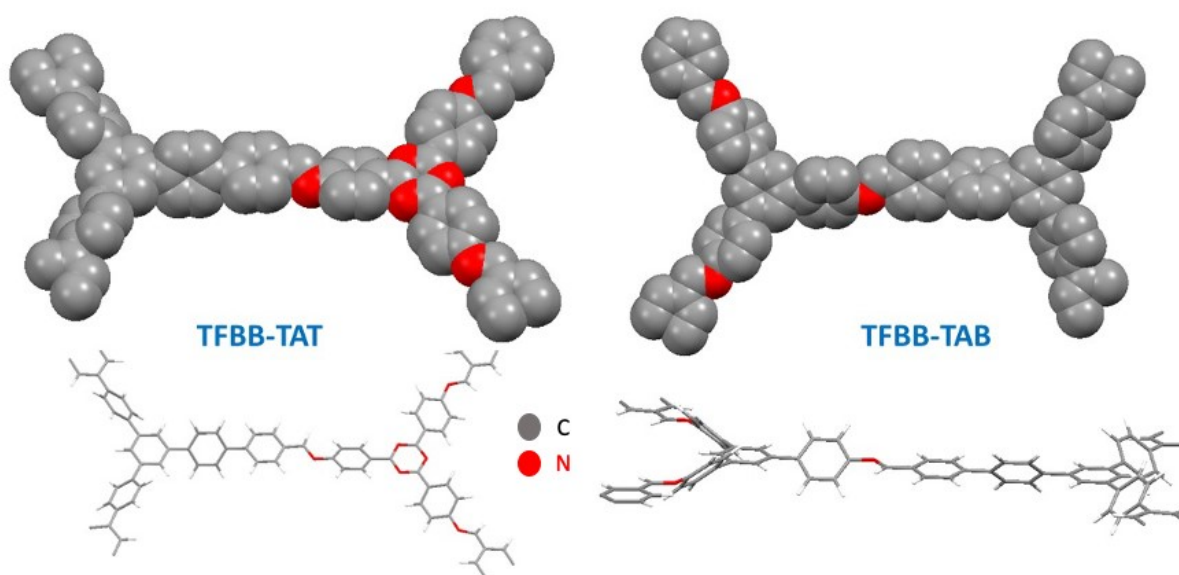

Figure S13. Monomer unit of TFBB-TAT COF and TFBB-TAB COF .

Table T1. Energies, stabilization energies, interlayer distances and band gaps of optimized TFBB-TAT structures

	Interlayer distance (Å)	Total Energy (a.u.)	LJ energy (a.u)	Per layer stabilization (kcal/mol)	HOMO-LUMO gap (eV)
monolayer		-143.036403	0.6244		2.704

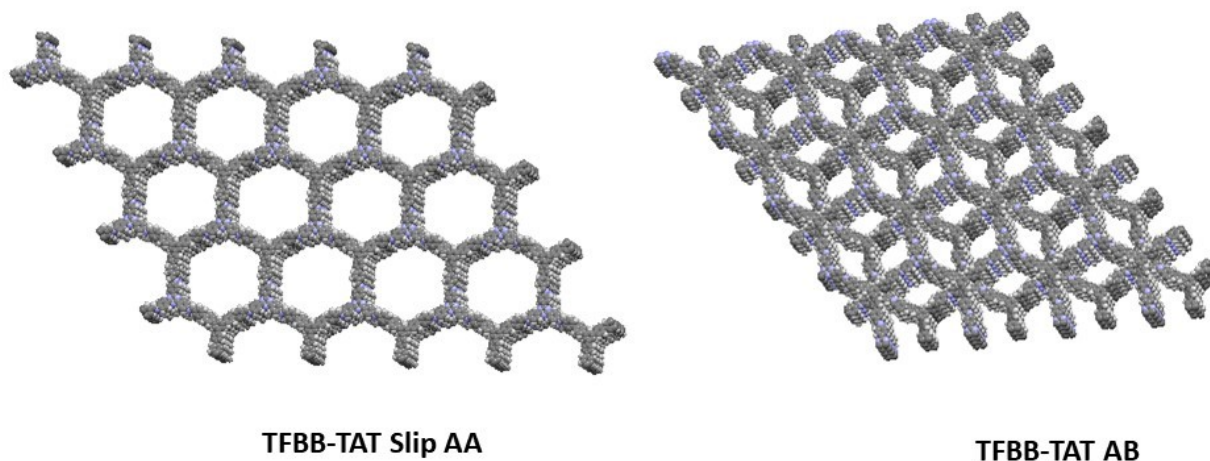|					
AA	3.58	-286.319952	0.9983	-77.54	2.336
slipAA	3.58	-286.338211	0.9858	-83.27	2.413
AB	3.19	-286.183072	1.1452	-34.60	2.411

TFBB-TAT Slip AA

TFBB-TAT AB

Figure S14. Structure of Slipped AA and AB of TFBB-TAT COF.

Table T2. Energies, stabilization energies, interlayer distances and band gaps of optimized TFBB-TAB structures

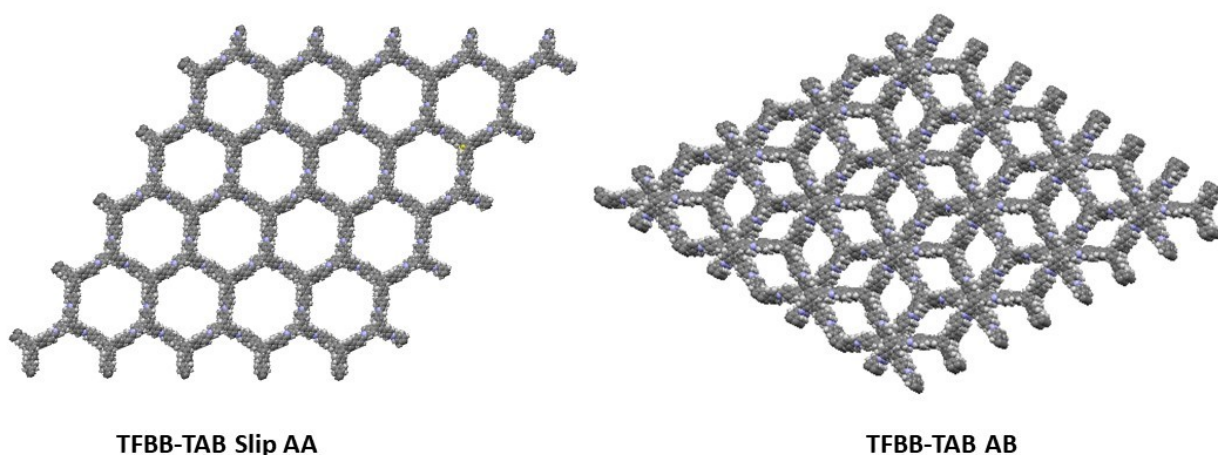|	Interlayer distance (Å)	Total Energy (a.u.)	LJ energy (a.u)	Per layer stabilization (kcal/mol)	HOMO-LUMO gap (eV)
monolayer		-142.186638	0.6400		2.638
AA	3.60	-284.612583	1.0398	-75.08	2.156
slipAA	3.61	-284.625001	1.0234	-78.98	2.235
AB	3.29	-284.485398	1.1777	-35.18	2.371

TFBB-TAB Slip AA

TFBB-TAB AB

Figure S15. Structure of Slipped AA and AB of TFBB-TAB COF.
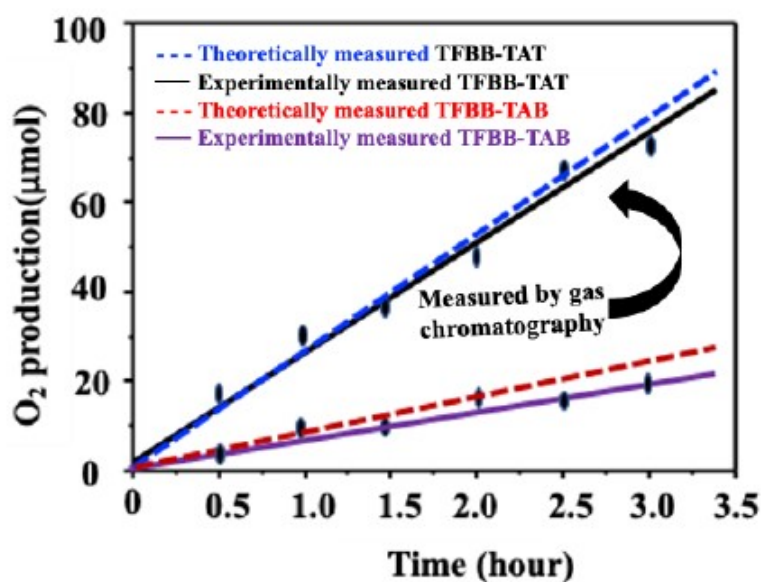
Figure S16. Oxygen production rate through PEC water splitting reaction for (a) TFBB-TAT and (b) TFBB-TAB COF

Table T3: Comparison of the Photocurrent density activity of the metal free TFBB-TAT with other reported materials in literature:

Material	Photocurrent density (mA/cm^2)	at Potential vs RHE (V)	Experiment condition	Reference
p-Si/C3N4−CoSe2	−4.89	0	0.5 M H_2SO_4	[1]

CIGS/CdS/ZnO	−32.5	−0.7	1 M KOH (pH 9)	[2]
MoS2	15.7	0	0.5 M H_2SO_4	[3]
TiO_2 /MOF	32X10^{-4}	0.75	0.5 M Na_2SO_4 (pH 6.5)	[4]
Cu2S	7.0	−0.3	0.5 M Na_2SO_4 and 0.1 M KH_2PO_4 (pH 5)	[5]
GaN nanowire	−31	−0.2	1 M H_2SO_4	[6]
Pt/TiN/n$^+$p-Si	10	-0.15	0.5 M H_2SO_4	[7]
Ru/CTGS (Ru/$Cu_2Sn_{0.38}Ge_{0.62}S_3$)	6.0	0	1.0 M potassium phosphate	[8]
ITO/ BDT-ETTA/Pt	3~4	0.96	0.1 M Na_2SO_4	[9]
FTO/CuSCN/P3HT/TPBMeOTP-NP/SnO2/Pt	17	1.06	0.5 M NaH2PO4	[10]
TFBB-TAT	4.32	0	0.5 M Na_2SO_4	This work

References:

1. S. K. Das, S. Mishra, K. Manna, U. Kayal, S. Mahapatra, K. D. Saha, S. Dalapati, G. P. Das, A. A. Mostafa, A. Bhaumik, *Chem. Commun.,* 2018, **54**, 11475.

2. TFBB-TAB Slip AA TFBB-TAB ABS9 B. Aradi, B. Hourahine, Frauenheim. Th., DFTB+, a sparse matrix-based implementation of the DFTB method, *J. Phys. Chem. A*, 2007, **111**, 5678.

3. M. Elstner, D. Porezag, G. Jungnickel, J. Elsner, M. Haugk, Th. Frauenheim, S., Suhai, G. Seifert, P*hys. Rev. B*, 1998, **58**, 7260.

4. B. Lukose, A. Kuc, T. Heine, *Chem. Eur. J.,* 2011, **17**, 2388

5. M. Basu, Z. W. Zhang, C. J. Chen, T. H. Lu, S. F. Hu and Ru-Shi. Liu, *ACS Appl. Mater. Interfaces,* 2016, **8**, 26690−26696.

6. M. G. Mali, H. Yoon, B. N. Joshi, H. Park, S. S. Al-Deyab, D. C. Lim, S. Ahn, C. Nervi, and S. S. Yoon, *ACS Appl. Mater. Interfaces,* 2015, **7**, 21619−21625

7. L. A. King, T. R. Hellstern, J. Park, R. Sinclair and T. F. Jaramillo, *ACS Appl. Mater. Interfaces*, 2017, **9**, 36792−36798.

8. L. Zhang, P. Cui, H. Yang, J. Chen, F. Xiao, Y. Guo, Y. Liu, W. Zhang, F. Huo and B. Liu, *Adv. Sci.,* 2016, **3**, 1500243.

9. Y. X. Yu, L. Pan, M. K. Son, M. T. Mayer, W. D. Zhang, A. Hagfeldt, J. Luo and M. Grätzel, *ACS Energy Lett.,* 2018, **3**, 760−766.

10. P. Varadhan, H. C. Fu, D. Priante, J. R. D. Retamal, C. Zhao, M. Ebaid, T. K. Ng, I. Ajia, S. Mitra, I. S. Roqan, B. S. Ooi and J. H. He, *Nano Lett.,* 2017, **17**, 1520−1528.

11. S. Hwang, S. H. Porter, A. B. Laursen, H. Yang, M. Li, V. Manichev, K U. D. Calvinho, V. Amarasinghe, M. Greenblatt, E. Garfunkeland G. C. Dismukes, *J. Mater. Chem. A,* 2019, **7**, 2400-2411

12. Y. Kageshima, S. Shiga, T. Ode, F.Takagi, H.Shiiba, M. T. Htay, Y.Hashimoto, K.Teshima, K.Domen, and H. Nishikiori *J. Am. Chem. Soc.* 2021, **143**, 5698.

13. T. Sick, A. G. Hufnagel, J. Kampmann, I. Kondofersky, M. Calik, J. M. Rotter, A. Evans, M. Döblinger, S. Herbert, K. Peters, D. Böhm, P. Knochel, D. D. Medina, D. F. Rohlfing, and T. Bein, *J. Am. Chem. Soc.* 2018, **140**, 6, 2085.

14. L. Yao, A. R. Camargo, M. Xia, D. Mücke, R. Guntermann, Y. Liu, L. Grunenberg, A. J.Solano, S. T. Emmerling, V. Duppel, K. Sivula, T. Bein, H. Qi, U. Kaiser, M. Grätzel, and B. V. Lotsch, *J. Am. Chem. Soc.* 2022, **144**, 10291.